

Volume 6 Paper H047

Controlled Oxidation of *M*CrAlY Coatings at Low Pressures

L.P.H. Jeurgens*, T.J. Nijdam and W.G.Sloof#

Department of Materials Science and Engineering, Delft University of Technology, Rotterdamseweg 137, 2628 AL Delft, The Netherlands.

* Present address: Max Planck Institute for Metals Research, Heisenbergstrasse 3, D-70569 Stuttgart, Germany.

Corresponding author: Dr. W.G. Sloof (phone: +31 15 278 4294; fax: +31 15 278 6730; email: W.G.Sloof@tnw.tudelft.nl).

Abstract

The effect of partial oxygen pressure and a native oxide on the structure, morphology and chemical constitution of the initial oxide layer grown on a *M*CrAlY bond coat was investigated. To this end, a state-of-the-art Ni-19Co-18Cr-21Al-0.2Y (at.%) bond coat, as prepared by electron beam physical vapour deposition, was oxidised in a UHV reaction chamber, with or without its native oxide, at 1373 K and a partial oxygen pressure of 0.1 Pa. The structure, morphology and chemical constitution of the initially grown oxide layer, as well as the oxidation-induced changes within the coating, were characterised using a broad range of analytical techniques. Special attention was paid to differences in the distribution of Y and the presence of any non-protective oxide phases within the initially grown oxide layer. The results were compared with a corresponding oxidation treatment at atmospheric conditions in a conventional tube furnace. It is shown that the exclusive formation of a continuous, closed α -Al₂O₃ layer with a strong Y-enrichment at its outer surface is promoted at low partial oxygen pressure and in the absence of a native oxide.

Keywords: *M*CrAlY bond coat, pre-treatment, oxidation, annealing, Y segregation and distribution.

1. Introduction

In modern high-temperature (> 1273 K) coating systems, $M\text{CrAlY}$ ($M = \text{Ni, Co}$) alloys are used as a bond coat between a ceramic thermal barrier topcoat (TBC) and the Ni-base superalloy component, such as a blade or vane in a gas turbine engine (cf. [1,2]). The superalloy is designed to provide the mechanical strength of the load-bearing components at high operating temperatures. The TBC, in conjunction with component cooling, serves to reduce the component-surface temperature up to about 150 K (cf. [3]), thereby allowing a higher operating temperature, which results in an enhanced efficiency of energy conversion.

The susceptibility to cracking and spalling of the coating system in service mainly relies on the capability of the $M\text{CrAlY}$ bond coat to produce and maintain a protective (i.e. stable, adherent, slow-growing) $\alpha\text{-Al}_2\text{O}_3$ layer, since the TBC is highly oxygen-transparent. In practice, the $M\text{CrAlY}$ bond coat is already oxidised upon deposition of the TBC in the fabrication process. Although the structure, morphology and chemical composition of the resulting, initial oxide layer are crucial for the subsequent formation and continued growth of a protective and adherent $\alpha\text{-Al}_2\text{O}_3$ layer on the bond coat during service, these aspects are nearly always poorly defined and controlled.

Therefore, the effect of different, *controlled* oxidation or annealing treatments of a $M\text{CrAlY}$ coating on the structure, morphology and chemical composition of the resulting, initially grown oxide layer, was investigated. To this end, a state-of-the-art dual-phase Ni-19Co-18Cr-21Al-0.2Y (at.%) coating, as prepared by Electron-Beam Physical Vapour Deposition (EB-PVD), was annealed or oxidised in a UHV reaction chamber at a temperature of 1373 K in pure argon or oxygen gas at a pressure of 0.1 Pa, respectively. To study the effect of the presence of a native oxide film on the coating surface, the treatments were repeated for the sputtered-clean coating surface. The results for the controlled oxidations executed in the UHV reaction chamber at a low partial oxygen pressure ($p\text{O}_2$) were compared with a corresponding oxidation treatment at atmospheric conditions in a conventional tube furnace.

The microstructure, oxide phase constitution and chemical composition of the grown oxide layers were investigated using X-ray Photoelectron Spectroscopy (XPS), Auger Electron Spectroscopy (AES), Transmission Electron Microscopy (TEM), Secondary Ion Mass Spectrometry (SIMS) and X-ray Diffractometry (XRD). The oxide-layer thickness, morphology and architecture were analysed with Light Optical Microscopy (LOM) and Scanning Electron Microscopy (SEM) in combination with X-ray microanalysis. Special attention was paid to differences in the distribution of Y and the presence of any non-protective oxide phases within the initially grown oxide layer.

2. Experimental

2.1. Material

A 2 mm thick dual-phase NiCoCrAlY coating was produced by EB-PVD deposition of an as-cast Ni-20Co-20Cr-22Al-0.2Y (at.%) alloy. After the deposition process, the coating was densified by shot-peening and subsequently stress-relieved by annealing for 2 h at 1353 K in a vacuum oven (i.e. system pressure ~ 0.1 Pa). The resulting coating has a very low porosity and possesses a fine-grained, columnar structure, consisting of a brittle Al-rich/Cr-poor β -phase (bcc) and a more ductile Al-poor/Cr-rich γ -phase (fcc). The typical width and length of the columnar grains is about 1 μm and 50 μm , respectively. The nominal composition of the coating, as determined by EPMA (see Sec. 2.4), was Ni-19Co-18Cr-21Al-0.2Y (at.%). The corresponding compositions of the γ - and β -phase were Ni-20Co-26Cr-11Al (at.%) and Ni-20Co-8Cr-33Al (at.%), respectively. The concentration of Y within the γ and β -phase was below the detection limit of the EPMA (i.e. < 85 ppm). The Y was homogeneously distributed as YNi-rich intermetallic precipitates at the γ/β -phase boundaries within the coating.

2.2. Sample Preparation

Disc-shaped specimens (diameter 10 mm and thickness 1 mm) were cut using spark-erosion. Prior to oxidation, the specimen surface was prepared by grinding, lapping and polishing, successively. Polishing was performed with a paste of 3 μm , then 1 μm and finally 0.25 μm diamond grains. Thereafter, the surface was fine-polished, using a chemical resistant cloth with a suspension of 0.04 μm silica in distilled water. After each preparation step the specimens were thoroughly cleaned ultrasonically with isopropanol and dried by blowing with pure compressed nitrogen gas.

For the preparation of the oxide/coating cross-sections, first a copper or gold layer was deposited on the grown oxide layer by evaporation or sputtering, respectively. Then, a nickel layer was electroplated on top of the copper layer using a Watts bath. Next, the specimen was cut perpendicular to its surface with a diamond saw. Finally, the oxide/coating cross-sections were ground and polished as described above.

For the preparation of the TEM sample, a 1 mm thick glass plate was glued on the Ni plated side of the specimen (see above) prior to the cutting. Both sides of the cross section were mechanically ground and polished until the slide had attained a thickness of about 15 μm . Then, the slide was put onto a Cu slot grid. Finally, both sides of the cross-section were ion milled (GATAN Precision Ion Polishing System, type 691) using a 4 keV Ar^+ beam at an angle of 3-5° with respect to the surface until a hole was formed. Then, at the edge of the hole, electron transparent areas were present for TEM analysis of the oxide/coating cross-section.

2.3. Oxidation and Annealing

The low $p\text{O}_2$ oxidation experiments, as well as the annealing treatments, were performed at 1373 K in a UHV reaction chamber (base pressure $< 10^{-7}$ Pa) coupled to an instrument for XPS analysis (base pressure $< 10^{-8}$ Pa). In some cases, the native oxide film (a few nm thick), consisting of Ni, Al and Cr oxides with adventitious C on top, was removed prior to oxidation or annealing by sputtering for 1 hour with a

focused 4 keV Ar⁺ beam scanning the surface area. Next, the specimens were heated within 5 minutes to 1373 K in pure argon gas (99.998 vol.% Ar) at 0.1 Pa. Then, the coating was either annealed in pure argon gas (99.998 vol.%) at 0.1 Pa or oxidised by exposure to pure oxygen gas (99.998 vol.%) at 0.1 Pa.

The high $p\text{O}_2$ oxidation experiment was performed at 1373 K (or 1273 K) in a horizontal alumina tube furnace (Lenton PTF 16/75/610; tube inner diameter 75 mm). A gas mixture of argon (99.998 vol.% Ar) and 20 vol.% oxygen gas (99.998 vol.% O₂) was passed through the furnace, at a total pressure of 10⁵ Pa (i.e. $p\text{O}_2 = 2 \times 10^4$ Pa), with a controlled flow rate of 750 ml/min. Before mixing, both gasses were passed through a moisture filter and a charcoal filter. The specimens were placed in an annealed alumina crucible and transported to the hot zone of the furnace, which is at the oxidising temperature of 1373 K.

2.4. Analysis and Data Evaluation

The coating composition (see Sec. 2.1) was determined with EPMA using a JEOL JXA 8900R WD/ED combined microanalyzer, equipped with five wavelength-dispersive spectrometers (WDS) (see [4] for details).

The chemical constitution at the oxidised or annealed coating surface was determined with XPS. Spectra were recorded with a PHI 5400 ESCA instrument, equipped with a spherical capacitor analyser, set at constant analyser pass energy of 71.55 eV, and with a step size of 0.125 eV, using unmonochromatised Al or Mg X-ray radiation. The emitted electrons were detected at an angle of 45° with respect to the specimen surface.

XRD was employed to determine the crystalline phases present in the grown oxide layers. The diffraction experiments were performed with a Bruker AXS D5005 θ - θ diffractometer using monochromatic Cu K α radiation and applying sample rotation. The samples were analysed in the 2θ range 20-80° with a step size of 0.050°. For phase identification the JCPDS database was used (JCPDS-International Center for Diffraction Data, Swarthmore, PA).

In some cases, the element distribution as a function of depth below the oxide surface was determined by SIMS or AES depth profiling. For the AES analysis, the Ni LMM, Cr LMM, Co LMM, Al KLL, Y MNN, O KLL and C KLL peaks were recorded with a PHI 4300 scanning Auger electron microscope using a primary electron beam of 5 keV and 1 μA , and employing a sputter interval of 1 minute (4 keV Ar⁺ beam; 3x3 mm² raster; with Zalar rotation). To resolve the concentration-depth profiles of the elements in the oxide layer and the coating, first the intensities of the corresponding oxidic and metallic components in the measured spectra were resolved as a function of depth below the surface by Factor Analysis (FA) of the background corrected, normalised spectra (see Ref. [5] for details). Next, the corresponding concentration-depth profiles were obtained by multiplying the resolved metallic and oxidic intensities of each element with their sensitivity factor and normalising to 100 at.%.

For the SIMS sputter-depth profiling, a 2 keV Ar⁺ beam in spot mode was focused on the oxidised surface and the emitted Al, Ni, Co, Cr and Y secondary ions were analysed using a quadrupole mass spectrometer (Balzers QMA 430) equipped with a

three-lens ion optics systems and a secondary electron multiplier (Balzers SEV 217). To reduce charging of the oxide layer during the SIMS analysis, a 20 nm thick gold layer was sputter-deposited on the oxidised surface, and any oxide layer present at the backside of the sample was removed by grinding. To visualize the distribution of the concerned elements as a function of depth below the oxidised surface, each recorded element intensity was multiplied with an arbitrary sensitivity factor, and subsequently normalised.

LOM and SEM analysis of the prepared oxide/coating cross-sections was applied to determine the morphology and architecture of the grown oxide layers. SEM analysis was performed with a JEOL JSM 6500F, equipped with an Energy-Dispersive Spectrometer (EDS) for quantitative composition analysis. The spectra acquisition and processing was performed with a ThermoNoran Vantage system.

The TEM analysis was performed with a Philips CM30T electron microscope, operated at an accelerating voltage of 300 kV. EDS analysis with a spot size in the range of 10 - 100 nm was applied to determine the composition at specific positions within the oxide layer and the underlying coating.

3. Results and Discussion

3.1. Oxidation-Induced Changes within Coating

Light optical and backscattered electron micrographs of cross-sections of the dual-phase Ni-19Co-18Cr-21Al-0.2Y (at.%) EB-PVD coating after three different oxidation treatments for 1 h at 1373 K are shown in Figs. 1 and 2, respectively. Clearly, a much thicker oxide layer has formed after oxidation for 1 hour in a conventional furnace at a relatively high pO_2 of 2×10^4 Pa than for the oxidations in a UHV reaction chamber at a low pO_2 of 0.1 Pa. Consequently, a stronger Al depletion has occurred (within the same period) for the oxidation at high pO_2 , leading to the transformation of the β -phase into the Al-poor γ -phase in the region contiguous to the oxide/coating interface (further denoted as γ^* -zone; cf. Fig. 1a).

For the oxidations at low pO_2 , the γ^* -zone is absent. Instead, for the oxidation of the coating with native oxide, the original dual-phase $\gamma + \beta$ structure of the coating is still preserved up to the oxide/coating interface (Fig. 1b), whereas for the oxidation of the sputtered-clean coating, a single-phase β region (i.e. Al-rich) has formed in the region contiguous to the oxide/coating interface (further denoted as β^* -zone; see Fig. 1c and Sec. 3.2).

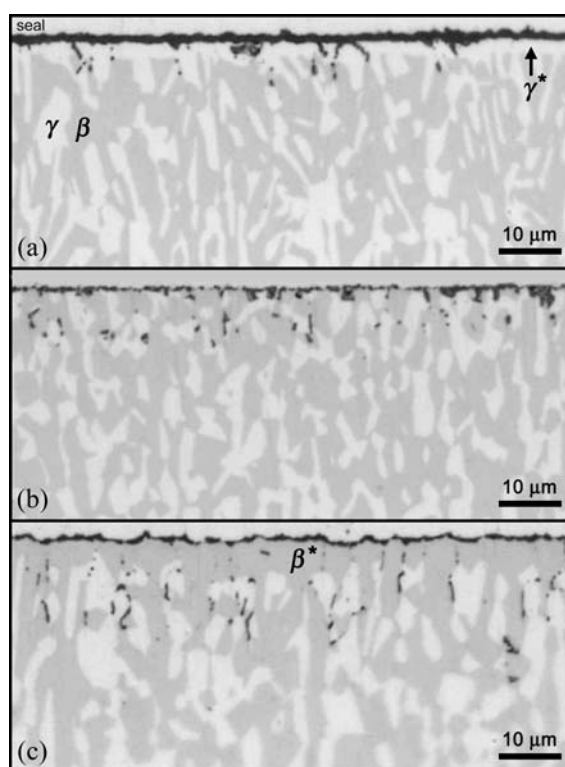


Figure 1. Light optical micrographs of a cross-section of the NiCoCrAlY coating (a) after oxidation in a furnace for 1 hour at 1373 K and $pO_2 = 2 \times 10^4$ Pa, (b) after oxidation in a UHV reaction chamber for 1 hour at 1373 K and $pO_2 = 0.1$ Pa, (c) after sputter-cleaning (i.e. removal of the native oxide) and subsequent oxidation in a UHV reaction chamber for 1 hour at 1373 K and $pO_2 = 0.1$ Pa. The light grey, dark grey and black areas correspond to the γ -phase, the β -phase and the oxide, respectively. In (a) a relatively thick oxide layer in combination with a near-surface, single-phase γ -zone (denoted as γ^* -zone) has formed, whereas in (c) the oxide layer is much thinner and a near-surface, single-phase β -zone (denoted as β^* -zone) is present. Also note the differences in the extent and depth of internal oxidation for the different treatments.

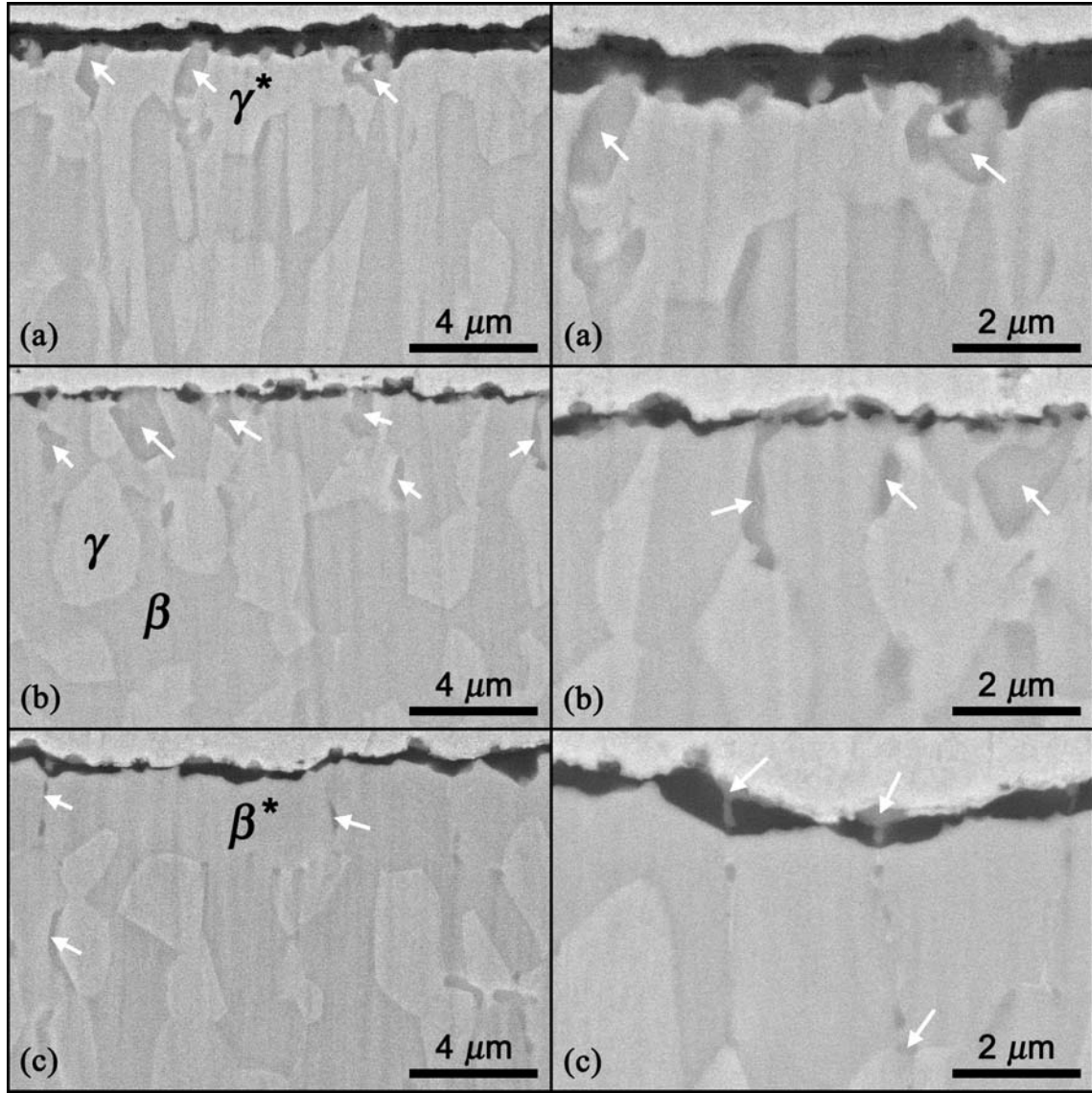


Figure 2. Backscattered electron micrographs (at two different magnifications) of cross-sections of the NiCoCrAlY coating (a) after oxidation in a furnace for 1 hour at 1373 K and $pO_2 = 2 \times 10^4$ Pa, (b) after oxidation in a UHV reaction chamber for 1 hour at 1373 K and $pO_2 = 0.1$ Pa, (c) after sputter-cleaning (i.e. removal of the native oxide) and subsequent oxidation in a UHV reaction chamber for 1 hour at 1373 K and $pO_2 = 0.1$ Pa. Some internal and external YAl-oxides have been indicated by the white arrows. See caption of Fig. 1 and text for details.

It is concluded that, for the high-temperature oxidation of a $M\text{CrAlY}$ coating, the oxide-layer growth kinetics and its associated Al depletion from the coating are suppressed at low pO_2 . As demonstrated in Ref. [4] for the high-temperature oxidation of γ -NiCrAl, a lower pO_2 reduces the activity of oxygen at the oxide/alloy interface during the initial, fast oxidation stage, thereby promoting the coalescence of initially grown $\alpha\text{-Al}_2\text{O}_3$ crystallites into a continuous closed $\alpha\text{-Al}_2\text{O}_3$ layer. Consequently, the duration of the initial, very fast oxidation stage and the associated Al depletion from the coating are suppressed. The presence of a native oxide layer on the coating may result in an additional, small decrease of the activity of oxygen at the native oxide/coating interface at the onset of oxidation.

3.2. Annealing-Induced Changes within Coating

For the sputtered-clean coating, no native oxide resides on the coating surface at the start of the oxidation in the UHV chamber. Due to the absence of the native oxide, extensive Cr evaporation occurs upon heating in UHV and subsequent oxidation at low pO_2 . As evidenced by LOM and SEM analysis of the coating after sputter-cleaning and subsequent annealing in the UHV chamber for 1 h at 1373 K (see Fig. 3), the Cr evaporation results in the transformation of the γ -phase into the Al-rich β -phase in the region contiguous to the oxide/coating interface (further denoted as β^* -zone), and a roughening of the parent coating surface. A corresponding annealing treatment of the coating *with* native oxide showed that the formation of the β^* -zone upon heating is suppressed in the presence of a native oxide.

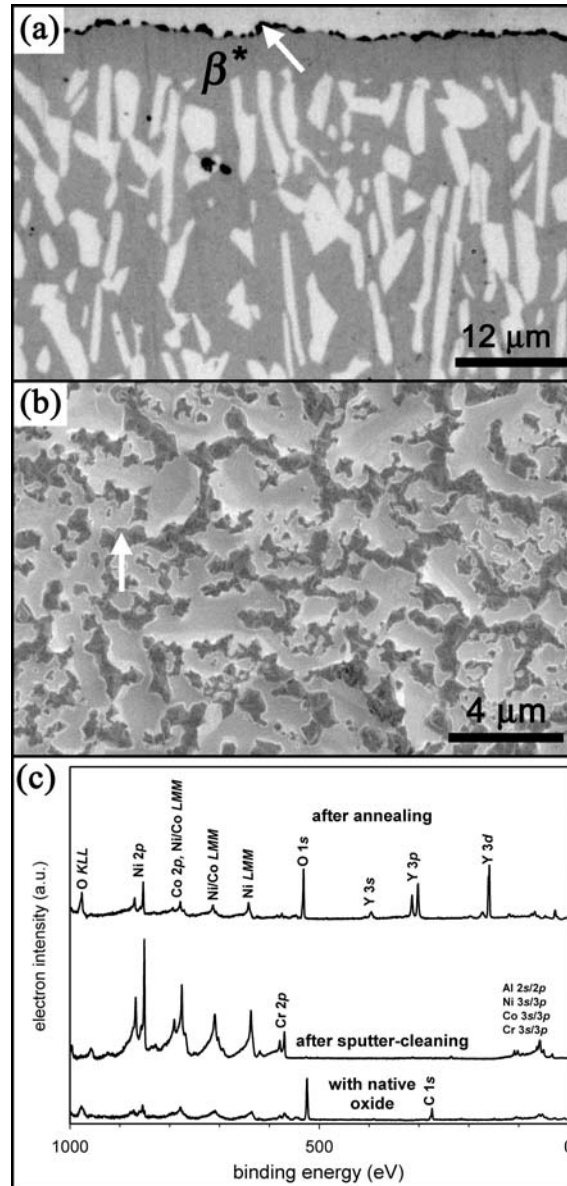


Figure 3. Light optical micrograph of a cross-section of the NiCoCrAlY coating after sputter-cleaning (i.e. removal of native oxide) and subsequent annealing for 1 hour at 1373 K in the UHV reaction chamber. (b) Secondary electron micrograph of the coating surface after the annealing. (c) Measured XPS spectra (after correction for X-ray satellites and inelastic background) recorded from the coating surface before and after sputter-cleaning, as well as after the annealing. As indicated by the XPS analysis, Y has segregated from the β^* -zone to the coating surface (white arrows) and has been partially oxidised (the Cr content at the annealed surface is negligible small).

3.3. Initial Segregation and Subsequent Distribution of Y

As evidenced by e.g. Figs. 1c and 2c, the YNi-rich intermetallic precipitates in the Cr-evaporation-induced β^* -zone, have dissolved upon the oxidation of the sputtered-clean coating at low pO_2 . XPS and SEM analysis of the annealed coating (Fig. 3c) showed that the Y has segregated from the β^* -zone along the original γ/β phase boundaries to the coating surface. As a result, upon subsequent oxidation, the internal oxidation zone of YAl-oxides (see below) is concentrated below the Y-depleted β^* -zone (Fig. 1c) and the developing oxide layer is covered with a noticeable thin layer of Y_2O_3 [6] (see Figs. 2c and 4).

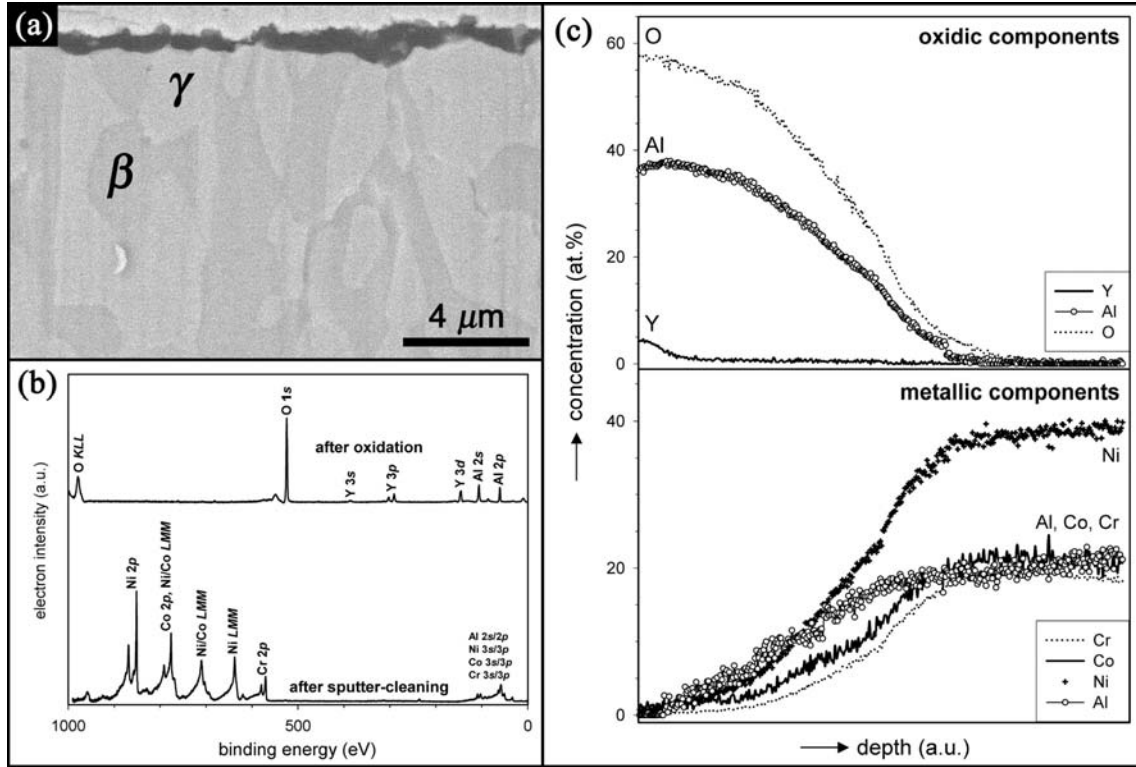


Figure 4. (a) Backscattered electron micrograph of a cross-section of the NiCoCrAlY coating after sputter-cleaning (i.e. removal of native oxide) and subsequent oxidation for 4 h at 1373 K and $pO_2 = 0.1$ Pa in the UHV reaction chamber. (b) Measured XPS spectra (after correction for X-ray satellites and inelastic background) recorded from the oxidised surface after sputter-cleaning and after subsequent oxidation. (c) Concentration of the oxidic and metallic components as a function of depth below the oxide surface, as resolved from the measured sputter-depth profile recorded from the oxidised coating using AES. As indicated by the XPS and AES analysis, the grown oxide layer is constituted of Al with some Y, and has a strong Y enrichment at its outer surface.

The formation of a Y-depleted β^* -zone, in combination with a strong Y-enrichment at the outer oxide surface, is suppressed by the presence of a native oxide on the coating at the onset of the oxidation. Instead, segregated Y becomes concentrated as large pegs of $Y_3Al_5O_{12}$ [7] (and some $AlYO_3$ [8]), extending from the outer surface along γ/β phase boundaries into the $\gamma+\beta$ interface region of the coating (cf. Fig. 2b). Consequently, the developing $\alpha-Al_2O_3$ [9] layer is less compact (i.e. less dense) and less uniform of thickness than for the sputtered-clean coating (cf. compare Fig. 1b and c).

The observed differences in oxide-layer morphology and constitution, for the oxidation of the coating with or without a native oxide at low pO_2 , are attributed to the differences in the extent of Y segregation at the onset of the oxidation, and the resulting distribution of Y within the initially grown oxide layer. For example, the presence of initially segregated Y at the coating surface, as well as Cr-evaporation-induced roughening of the coating surface, may result in a higher density of heterogeneous nucleation sites for the formation of $\alpha-Al_2O_3$ [10, 11]. Consequently, the coalescence of the initial $\alpha-Al_2O_3$ crystallites into a closed $\alpha-Al_2O_3$ layer is promoted for the oxidation of the sputtered-clean coating (cf. compare Fig. 1b and c).

For the oxidation of the coating with native oxide at *high* pO_2 , no Y is detected at the oxide surface (Fig. 5c) or in the oxide subsurface region (Fig. 5d), indicating that

virtually no Y segregation has occurred at the onset of the oxidation. Instead, subsequently segregated Y becomes concentrated as large pegs of $Y_3Al_5O_{12}$ (and some $AlYO_3$), extending from the oxide/coating interface (i.e. below the initially grown oxide layer) along original γ/β phase boundaries into the γ^* -region of the coating (cf. Fig. 5).

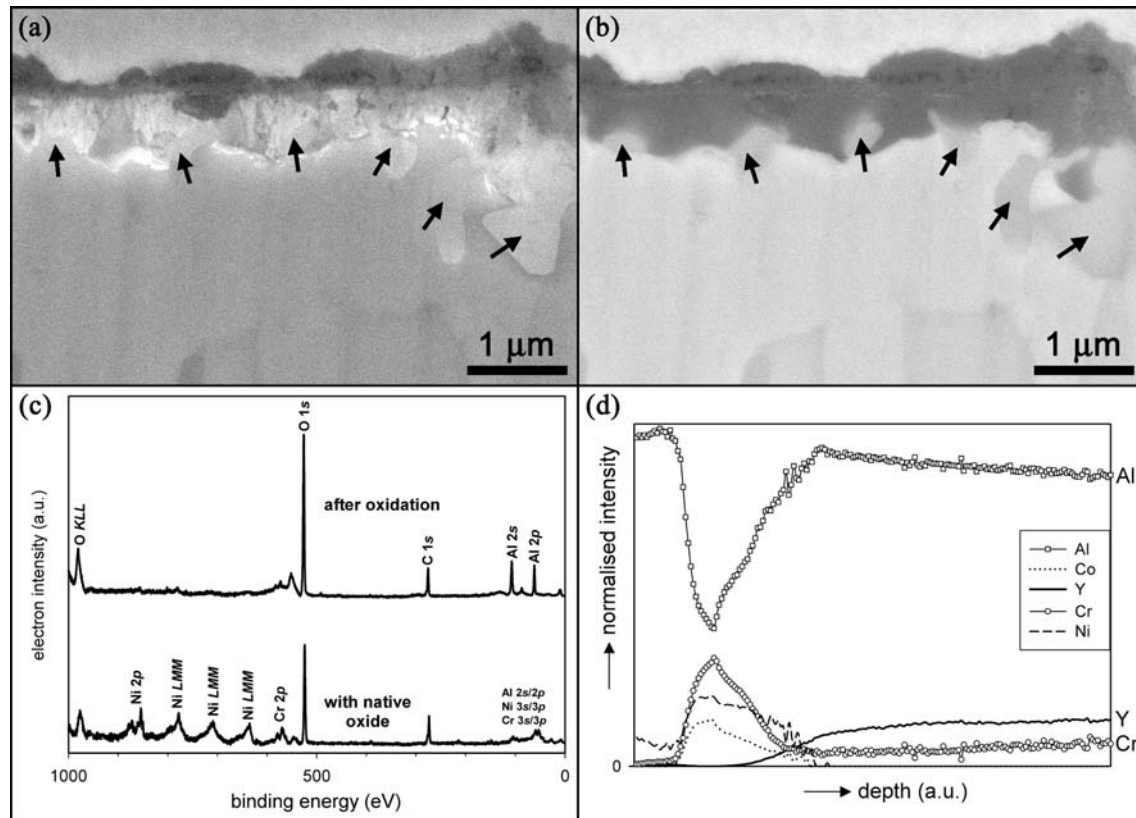


Figure 5. (a) Secondary electron micrograph and (b) corresponding backscattered electron micrograph of a cross-section of the NiCoCrAlY coating after oxidation in a furnace for 1 hour at 1373 K and $pO_2 = 2 \times 10^{-4}$ Pa. The AlY-oxide pegs at the oxide/coating interface have been indicated by the black arrows. (c) Measured XPS spectra (after correction for X-ray satellites and inelastic background) recorded from the oxidised surface before and after the oxidation. Only Al-oxide with small amounts of (Ni, Al, Cr)-oxide is detected at the oxidised surface. (d) Normalised intensity of Al, Co, Y, Cr and Ni as a function of depth below the oxide surface, as resolved from the measured sputter-depth profile recorded from the upper part of the grown oxide layer using SIMS. The surface-adjacent part of the top oxide layer, corresponding to the *dark* layer in (a), is constituted of Al, Cr, Ni and Co (with a strong Al-enrichment at its very surface), whereas the upper part of bottom oxide layer, corresponding to the *bright* layer in (a), consists of Al with small amounts of Cr and Y.

It is concluded that the initial segregation of Y to the coating surface at the onset of the high-temperature oxidation of the coating, as well as the resulting Y-enrichment at the outer surface of the developing oxide layer, are promoted at low pO_2 and in the absence of a native oxide layer. Then, the subsequent formation of large pegs of $Y_3Al_5O_{12}$ (and some $AlYO_3$) at the oxide/coating interface is suppressed.

3.4. Internal Oxidation of Y

For all three oxidation treatments, internal oxidation of the YNi-rich intermetallic precipitates, which are concentrated at original γ/β phase boundaries in the coating,

has occurred through inward diffusion of oxygen along original γ/β phase boundaries (Fig. 1). XRD analysis of the oxidised specimens in combination with EDS analysis of their cross-sections in the SEM, show that these internal oxides are predominantly constituted of $\text{Y}_3\text{Al}_5\text{O}_{12}$ with some AlYO_3 . The internal oxidation of the YNi-rich precipitates in the coating results from the higher inward flux of oxygen along original γ/β phase boundaries as compared to the outward flux of Y along these boundaries (as determined by the rate of dissolution and subsequent segregation).

For the oxidations at low $p\text{O}_2$ in a UHV chamber, SEM analysis of the oxide/coating cross-sections often reveals paths of $\text{Y}_3\text{Al}_5\text{O}_{12}$ (and some AlYO_3) running from the oxide/coating interface through the developing $\alpha\text{-Al}_2\text{O}_3$ layer to an outer surface, which is mainly constituted of Y_2O_3 (cf. Figs. 2b and c). These features are confined to positions above original γ/β phase boundaries, where dissolution and subsequent segregation of Y to the coating surface, as well as internal oxidation of YNi-rich intermetallic precipitates, has occurred. These YAl-oxide paths are much less pronounced for the oxidation of the *sputtered-clean* coating at low $p\text{O}_2$ (which initially forms an Y-depleted β^* -zone) and were not observed for the oxidation of the coating *with* native oxide at high $p\text{O}_2$ (for which initial Y segregation is hindered). The presence of these YAl-oxide paths within the grown oxide layer (for the oxidations at low $p\text{O}_2$) indicate that dissolution and segregation of Y along original γ/β phase boundaries to the oxide/coating interface, followed by outward diffusion of Y along oxide grain boundaries to the oxide surface, has occurred during the oxidation. The outward diffusion of Y through the oxide is driven by the oxygen potential gradient across the developing oxide layer [11, 12]. However, an additional driving force must be responsible for the dissolution and segregation of Y from the interior of the coating to the oxide/coating interface, since this process also takes place in the absence of an oxygen potential gradient (i.e. upon annealing in UHV; see Sec. 3.2). In the absence of an oxygen potential gradient, the dissolution and segregation of Y to an alloy surface is generally attributed to the high lattice strain energy associated with the size mismatch of the relatively large Y atoms within the alloy [10, 11]. The outward diffusion of Y along alloy and oxide grain boundaries hinders the outward transport of other, less reactive cations along these grain boundaries, and inhibits the formation and growth of voids at the oxide/coating interface [11, 12].

3.5. Distribution of Non-Protective Oxide Phases

After continued oxidation (i.e. after 4 h) of the sputtered-clean coating at low $p\text{O}_2$, the resulting oxide layer is constituted of $\alpha\text{-Al}_2\text{O}_3$ with the initially segregated and subsequently oxidised Y located at its surface (see Fig. 4); the β^* -zone has already partially transformed back into the γ -phase due to the oxidation-induced Al depletion. This contrasts with the oxidation of the coating *with* native oxide at high $p\text{O}_2$, for which a doubled-layered oxide structure has evolved (see Figs. 5a and 6). As revealed by XRD, SEM, TEM, XPS analysis and SIMS depth profiling (see Figs. 5 and 6), the top oxide layer (i.e. the dark layer in Fig. 5a) has a relatively fine-grained, equiaxed structure and is constituted of (spinel) oxides of Al, Cr, Ni and Co with a strong Al-enrichment at its very surface. The bottom oxide layer (i.e. the bright layer in Fig. 5a) has a denser, coarse-grained, columnar structure and consists of only $\alpha\text{-Al}_2\text{O}_3$ with small amounts of Cr and Y. The strong cathodoluminescence of the $\alpha\text{-Al}_2\text{O}_3$ bottom layer, as observed with the secondary electron detector (Fig. 5a), indicates that the

columnar α -Al₂O₃ grains are doped with Y (and Cr). The interface between the top and bottom oxide layer is relatively sharp, whereas the interface between the α -Al₂O₃ bottom layer and the coating is irregular due to the inward growth of α -Al₂O₃ and the formation of large YAl-oxide pegs at the oxide/coating interface by internal oxidation along original γ/β boundaries. This complies with the general view that the top oxide layer is grown mainly by the outward diffusion of metal cations, whereas the bottom oxide layer is grown predominantly by the inward diffusion of oxygen anions through the α -Al₂O₃ layer.

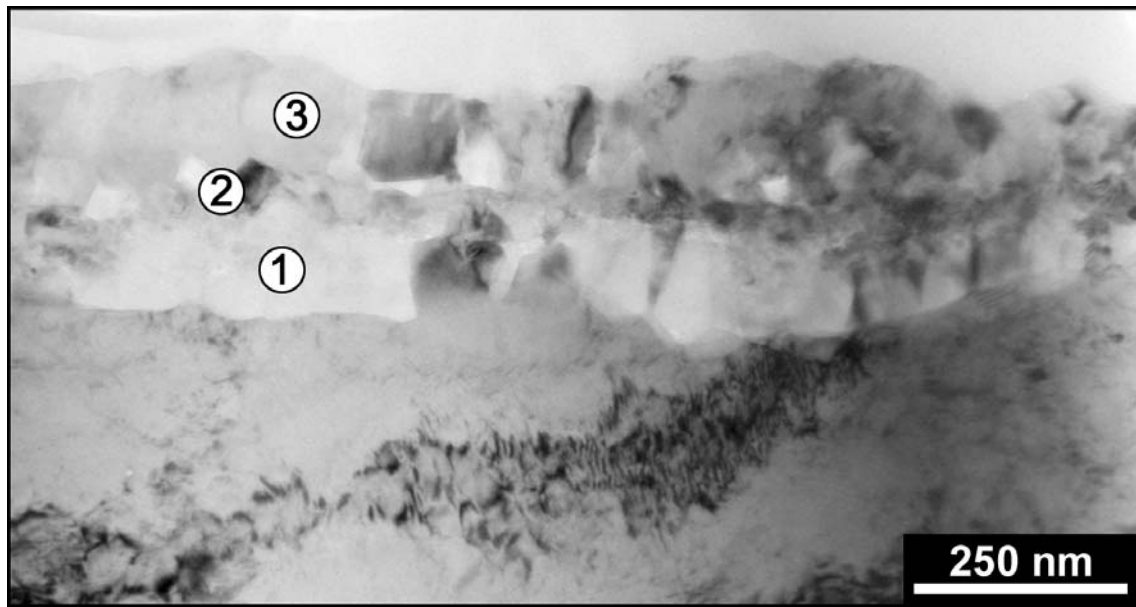


Figure 6. Transmission electron micrograph of a cross-section of the NiCoCrAlY coating after oxidation in a furnace for 0.5 hour at 1273 K and $pO_2 = 2 \times 10^{-4}$ Pa. Local EDS analysis revealed that the evolved double-layered oxide structure consists of a top oxide layer predominantly constituted of Al, Ni, Co, and Cr at its *upper* part (position 3) and Al and Cr at its *lower* part (position 2), and a relatively dense bottom layer of α -Al₂O₃ (position 1). See text for details.

As follows from the above discussion, the (micro)structure, morphology, constitution and chemical composition of the initial, thermally grown oxide layer on a MCrAlY bond coat is governed by its oxidation conditions (e.g. T and pO_2), as well as by its microstructure (e.g. Y-depleted β^* -zone) and surface condition (e.g. native oxide). It was shown that the distribution of Y within the coating, as well as within the developing oxide layer, is strongly dependent upon the partial oxygen pressure and the presence of a native oxide on the coating surface at the onset of oxidation. In general, it can be concluded that the rate of formation of a protective α -Al₂O₃ layer, with an Y-enrichment at its very surface, is enhanced for the oxidation of a MCrAlY coating at low pO_2 and in the absence of a native oxide layer. The influence of the Y-distribution within the initially grown oxide layer on the long-term performance of the entire coating system (i.e. superalloy substrate | bond coat | TBC; see Sec. 1) in service is still unknown. It is expected that a well-defined pre-treatment, consisting of controlled annealing and subsequent oxidation (prior to deposition of a TBC in the fabrication process), can have a beneficial effect on the durability of the coating system during service. This will be investigated by the present authors in the near future.

4. Conclusions

For the oxidation of a *M*CrAlY coating at 1373 K, the exclusive formation of a continuous, closed α -Al₂O₃ layer with a strong Y-enrichment at its outer surface is promoted at low $p\text{O}_2$ and in the absence of a native oxide.

A lower $p\text{O}_2$ reduces the activity of oxygen at the oxide/coating interface during the initial, fast oxidation stage, thereby promoting the coalescence of α -Al₂O₃ crystallites into a closed α -Al₂O₃ layer. Consequently, the duration of the initial, very fast oxidation stage and its associated Al depletion from the coating, as well as the formation of less-protective (spinel) oxides of Cr, Ni and Co, are strongly suppressed. In the absence of a native oxide and at low $p\text{O}_2$, the initial segregation of Y to the coating surface is promoted, resulting in a strong Y-enrichment at the developing oxide-layer surface and a limitation of the subsequent formation of large pegs of Y₃Al₅O₁₂ (and some AlYO₃) at the oxide/coating interface.

Upon the high-temperature oxidation of a *M*CrAlY coating, internal oxides of Y₃Al₅O₁₂ and AlYO₃ are grown at the γ/β phase boundaries by internal oxidation of YNi-rich intermetallic precipitates.

Heating and subsequent annealing of a *M*CrAlY coating at 1373 K in UHV results in the fast formation of a Y-depleted, single-phase β -zone in the region contiguous to the oxide/coating interface due to extensive Cr evaporation and strong Y segregation. The initial Y segregation and/or Cr-evaporation-induced roughening of the coating surface may promote the heterogeneous nucleation of α -Al₂O₃, thereby promoting the coalescence of the initial α -Al₂O₃ crystallites into a closed α -Al₂O₃ layer.

References

- [1] 'Designing Oxidation-Resistant Coatings', J.R. Nicholls, *JOM* , **52**, 1, pp.28-35, 2000.
- [2] 'Oxidation, Hot Corrosion and Protection of Metallic Materials', S.R.J. Saunders and J.R. Nicholls, *Physical Metallurgy (4th ed.)*, edited by R.W. Cahn and P. Haasen (Elsevier Science, Amsterdam), pp.1292-1361, 1996.
- [3] 'EB-PVD Thermal Barrier Coatings for Aeroengines and Gas Turbines', M. Peters, C. Leyens, U. Schulz and W.A. Kaysser, *Advanced Engineering Materials*, **3**, 4, pp.193-204, 2001.
- [4] 'Effect of Partial Oxygen Pressure on the Initial Stages of High-Temperature Oxidation of γ -NiCrAl Alloys', T.J. Nijdam, L.P.H. Jeurgens and W.G. Sloof, *Materials at high-temperatures*, in press, 2003.
- [5] 'Structure of thin aluminium-oxide films determined from valence band spectra measured using XPS', P.C. Snijders, L.P.H. Jeurgens and W.G. Sloof, *Surface Science*, **496**, pp.97-109, 2002.
- [6] Powder Diffraction file, 25-1200 from International Center for Diffraction Data (CDD).
- [7] Powder Diffraction file, 09-0310 from International Center for Diffraction Data (CDD).
- [8] Powder Diffraction file, 33-0041 from International Center for Diffraction Data (CDD).
- [9] Powder Diffraction file, 43-1484 from International Center for Diffraction Data (CDD).
- [10] 'Current viewpoints on oxide adherence mechanisms', J.L. Smialek and R. Browning, *Proceedings of the symposium on high temperature materials chemistry III*, edited by Z.A. Munir and D., Cubicciotti (Pennington, Electrochemical Society), pp.258-272, 1986.
- [11] 'Role of reactive elements in alloy protection', D.P. Moon, *Materials Science and Technology*, **5**, pp.754-764, 1989.
- [12] 'Experimental Observations in Support of the dynamic-segregation theory to explain the reactive-element effect', B.A. Pint, *Oxidation of Metals*, **45**, pp.1-37, 1996.